INTERNATIONAL ATOMIC ENERGY AGENCY
UNITED NATIONS EDUCATIONAL, SCIENTIFIC AND CULTURAL ORGANIZATION

INTERNATIONAL CENTRE FOR THEORETICAL PHYSICS
34100 TRIESTE (ITALY) - P.O.B. 586 - MIRAMARE - STRADA COSTIERA 11 - TELEPHONE 2240-1
CABLE: CENTRATOM - TELEX 460392-1

SMR/208 - 3

SPRING COLLEGE IN MATERIALS SCIENCE
ON
"METALLIC MATERIALS"
(11 May - 19 June 1987)

FIELD ION MICROSCOPY OF ALLOYS

P. HAASEN
Institut für Metallphysik der
Universität Göttingen
Hospitalstrasse 3
D-3400 Göttingen
Federal Republic of Germany

Ann. Rev. Mater. Sci. 1985. 15: 43-78

APPLICATION OF ANALYTICAL FIELD-ION MICROSCOPY TO THE DECOMPOSITION OF ALLOYS

P. Haasen[1]

Department of Materials Science and Engineering, Stanford University, Stanford, CA 94305

R. Wagner

Institut für Physik, GKSS Forschungszentrum, D2054 Geesthacht, and SFB 126 Göttingen-Clausthal, West Germany

INTRODUCTION

Many technologically important properties of alloys, such as mechanical strength, or the coercivity of ferromagnetic materials, are essentially controlled by the precipitate microstructure that results from the diffusion-controlled decomposition reaction of the originally supersaturated matrix. A fundamental understanding of the thermodynamics, the kinetics, and the mechanism of the phase transformation that leads to well-defined precipitate microstructures is, therefore, of great interest in metallurgy.

The course of a decomposition reaction, including the early stages (during which composition fluctuations and second-phase nuclei are formed) as well as the coarsening stages can generally *not* be followed continuously by any one microanalytical technique. The progress of a decomposition reaction is usually reconstructed from the microstructure that has developed at various stages of the phase transformation. Thus, it is

[1] On leave from Institut für Metallphysik, Universität Göttingen, D34 Göttingen, West Germany.

0084-6600/85/0801-0043$02.00

necessary to analyze the spatial extension and the amplitude of composition fluctuations of incipient, second-phase particles, as well as the morphology, number density, size, and chemical composition of discrete precipitates at various stages of the phase transformation. For this purpose microanalytical tools are required that are capable of resolving very small solute clusters, and simultaneously identifying their chemical composition.

Although the first requirement is frequently met by neutron (SANS) and X-ray (SAXS) small angle scattering techniques, and also by TEM (for particles larger than about 4 nm), the chemical analysis of particles smaller than about 12 nm is usually not possible using any of the standard microanalytical tools, such as the electron microprobe, or scanning transmission electron microscopy combined with an energy-dispersive X-ray analyzer.

This gap in the analysis of ultrafine precipitates can be bridged by employing the atom-probe field-ion microscope (AP FIM) (1), which is a combination of a field-ion microscope (FIM) and a time-of-flight mass spectrometer (atom-probe, AP). This instrument has the unique capability of imaging and identifying single atoms. For more than ten years the AP FIM has been used successfully for chemical analyses of, for example, individual carbide (2–4), or nitride precipitates (5) in various steels, and γ' particles in cast commercial nickel-based superalloys (6), which escaped detection by TEM [for a comprehensive review, see (7)]. These results are not treated again in this review.

The recent development of unified precipitation theories (8, 9), which treat nucleation, growth, and coarsening ("Ostwald ripening") as concurrent processes until precipitation is completed, has stimulated several AP FIM studies of the early stage precipitation kinetics in metastable supersaturated binary or ternary alloys. Some experimental results from those studies and their agreement with theoretical predictions are the subject of the second part of this article; various aspects of the AP FIM analysis of decomposing alloys are covered in the first part.

For many two-phase alloys the important theoretical question remains open of whether the phase transformation is initiated by the *formation of small nuclei* having a composition similar to that of the equilibrium phase (or at least similar to that of the intermediate metastable phase, which is formed in some alloys prior to the formation of the equilibrium phase), or whether it is initiated by *spinodal decomposition*. Since the latter reaction is caused by the thermodynamic instability of the quasi-uniform solid solution within the spinodal range (10–12), the decomposition occurs by the growth of three-dimensional composition waves without any nucleation barrier larger than $\sim kT$ to be overcome. The wavelengths of these long-range composition fluctuations are initially typically about 5 nm, but will

grow with aging time to tens of nm. According to various theories of spinodal decomposition (10, 11), the amplitudes of the composition waves increase gradually with aging time, starting from almost zero, until they reach a value corresponding to the concentration of the completely precipitated second phase.

The microstructures in the later transformation stages (where some of the conventional microanalytical tools can now be applied) evolve from either classical nucleation or spinodal decomposition, but do not necessarily differ from each other. Therefore, it is usually not accurate to deduce the mode of the initial decomposition reaction simply from observations of the microstructure in later transformation stages. The only way to prove experimentally that a solid solution decomposes spinodally is to show by a suitable microanalytical technique that the composition waves are gradually amplified during aging until discrete precipitates of the second phase have finally emerged.

As discussed in Section 1, in principle, long-range composition fluctuations can be analyzed with the atom-probe FIM, though sometimes statistical problems impede a straightforward interpretation of the measured composition profiles. The technique has been applied to study phase separation in a number of supersaturated alloys that are thought to decompose spinodally. This belief is based on some typical microstructural features (13), which, according to Cahn's phenomenological theory of spinodal decomposition (10), can—but do not necessarily—evolve from a spinodal reaction. Results and conclusions from some of these studies are discussed in Section 2.

1. EXPERIMENTAL ASPECTS

1.1 *Basic Design and Operation of an Atom-Probe FIM*

Since Müller and co-workers (18) conceived of and published the first design of an atom-probe FIM, several instruments specially developed for application to various metallurgical problems have been described in the literature (7, 14–17). Currently, about twelve instruments are being operated in metallurgical laboratories worldwide.

Figure 1 shows the basic features and electronic circuitry of an atom-probe FIM designed for the investigation of phase separation in alloys. Essentially, the instrument consists of two parts: the FIM to image the specimen, and the time-of-flight (ToF) spectrometer (the atom-probe) in which single ions, field evaporated from the FIM specimen surface, are identified. The imaging-screen contains in its center a probe-hole of about 2.5 mm in diameter. Field-evaporated ions, originating from the area covered by the projection of the probe-hole onto the specimen surface (the

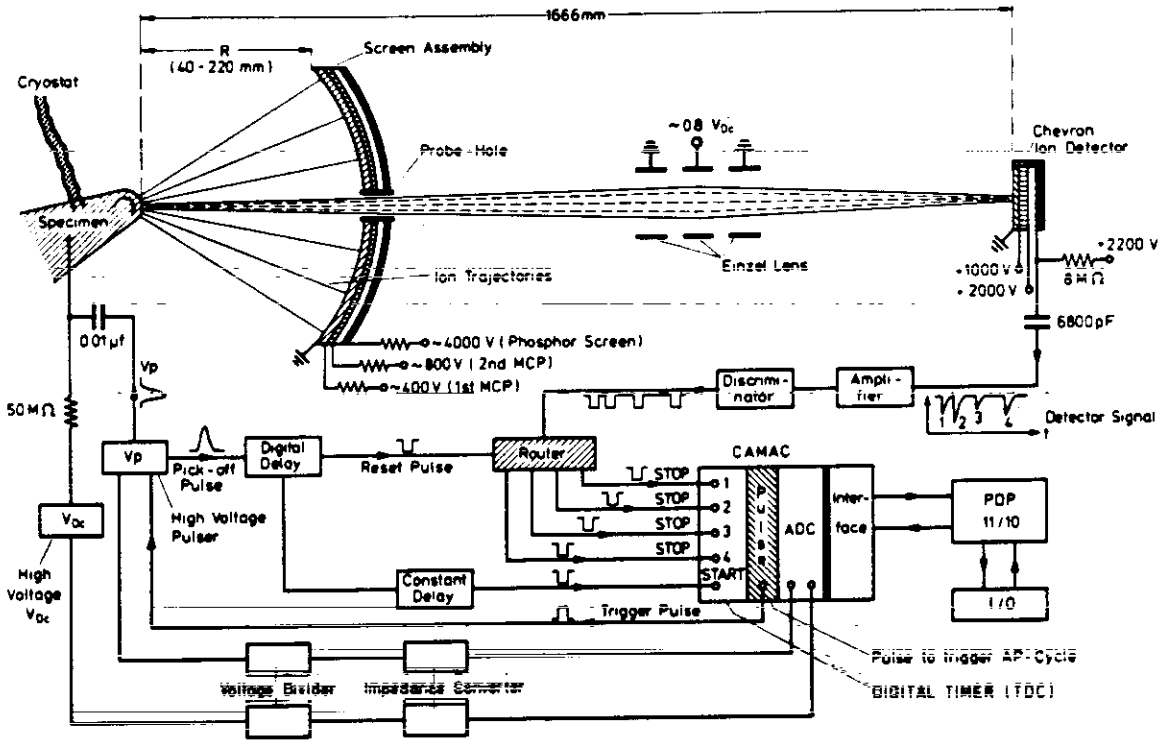

Figure 1 Atom-probe FIM operated at the University of Göttingen. The specimen is mounted on an x-y-z manipulator and attached to a cryostat filled with liquid N_2, via a flexible copper braid. The tip-to-screen distance (R) can be varied between 40–200 nm by shifting the FIM screen assembly (microchannel planes, MCP). The diameter of the probe-hole, which is internally grounded by a metal tube to avoid electrostatic deflections of the ion beam, is 2.5 mm. To maximize the ion yield per field-evaporated plane, the specimen is aligned with the instrument axis through x-y-z manipulation, until the current caused by randomly arriving imaging gas ions is at a maximum. The spread of the ion beam, which is imaged on the ion detector, is focused by adjusting the potential at the Einzel lens. Atom-probe control and data acquisition are performed by means of a computer that is interfaced to a CAMAC-system that consists of (*a*) a 4-channel 200-MHz clock (TDC) to measure the time-of-flight; the 4 channels of the clock are simultaneously started by a pulse which is synchronously picked off the high-voltage pulser. (*b*) A pulse module providing two pulses: (i) for triggering the high-voltage pulser, and thus, for initiating an atom-probe cycle, and (ii) to reset the router. If a sequence of ions (up to four), rather than a single ion, strikes the detector, the router assigns a stop signal from the first ion of the sequence to channel 1 of the TDC, the second one to channel 2, etc. (*c*) The AD converter (ADC) measures V_p and V_{DC} during each atom-probe cycle.

The vacuum system basically consists of the specimen exchange chamber and the main chamber, which contains the FIM; they are separated by a straight-through valve. For easy and rapid specimen exchange without spoiling the vacuum in the main chamber, 11 specimens can be stored on a revolving plate in the specimen chamber. With respect to the vacuum system, the only provision made to incorporate the time-of-flight spectrometer into the FIM is a flight-tube with a detector housing at its end (7).

"effective probe-hole area"), enter the flight-tube of the atom-probe through the probe-hole. At the end of the flight-tube the ions reach the single-ion detector.

The typical FIM specimen is a sharply pointed needle with a radius of curvature ($\bar{r}_t$) of about 20–80 nm. It is prepared from a thin wire of 0.1–0.3 mm diameter by anodic electropolishing (7). All heat treatments necessary for the particular phase transformation have to be performed prior to electropolishing.

After preparation, the specimen is introduced into the ultra-high ($\sim 10^{-9}$ mbar) vacuum chamber of the FIM via a specimen airlock, mounted onto a manipulator, and cooled to ~ 80 K in order to increase the resolution of the FIM image. The manipulator allows the specimen to be aligned along the axis of the instrument, and any region visible in the FIM image that is to be analyzed with the ToF spectrometer can be shifted until it covers the probe-hole of the atom-probe. The distance (R) between tip vertex and the center of the screen can be varied typically between ~ 4 and ~ 20 cm allowing for a variation of the "average" magnification ($\bar{M}$) in the FIM. $\bar{M}$ is given by

$$\bar{M} = \frac{R}{\bar{r}_t} \times \beta'. \qquad 1.$$

With typical values for the mean radius of curvature of the tip ($\bar{r}_t$)[2] and for R ($\sim 3 \times 10^{-2}$ cm and ~ 4 cm, respectively), $\bar{M}$ is on the order of 10^6. β' is approximately 0.6, which accounts for the fact that the FIM tip is not ideally hemispherical and, hence, the projection not purely gnomonic (18). Correspondingly, for the given values the effective diameter of the AP probe-hole (d_{ap}) can be varied between ~ 3.2 ($R \sim 4$ cm) and ~ 0.8 nm ($R \sim 20$ cm).

To obtain FIM images of the alloys referred to in this article, neon, the imaging gas, is leaked into the vacuum system ($\sim 5 \times 10^{-6}$ mbar). Subsequently, a positive high voltage (V_{DC}), typically between 3 and 20 kV depending on $\bar{r}_t$, is applied to the specimen. If the resulting electric field ($F \approx V_{DC}/\bar{r}_t$) exceeds a critical value ($F_c \approx 30$ V/nm) the neon atoms are positively ionized in the high field regions above the tip surface, and are accelerated almost radially toward the grounded FIM screen, which lights up at the points of impact.

Starting with a freshly prepared tip, the electric field is highest above the sharp protrusions retained from the specimen preparation. As the voltage is gradually increased, the electric field above these protusions reaches a value $F_{FE} > F_c$ at which local "field evaporation" (18) of individual atoms in the

[2] Both $\bar{r}_t$ and the local radius of curvature can be determined quite accurately directly from FIM micrographs (7).

form of n-fold charged ions occurs ($n = 1$ or 2 for most transition metals) (7). Since the onset of field evaporation occurs at a certain field strength, regions with smaller radii of curvature field evaporate earlier than those with larger ones. Thus, field evaporation is used to smooth a freshly prepared FIM specimen until the atomically smooth, curved tip-end required for ultimate resolution in the FIM images is finally obtained.

1.2 *Image Formation and Contrast of Decomposed Alloys*

The mechanism of image formation is illustrated in Figure 2. In the high-field regions of the FIM tip, the neon atoms become polarized and are therefore attracted to the positively charged tip surface. After several inelastic collisions with the cool surface, the polarized, hopping gas atoms are finally ionized by the tunneling of an electron from the gas atom through a potential barrier, and into the specimen. The tunnel probability is highest at a distance x_c, approximately 0.5 nm above the tip surface, where the energy of the electron lies at, or slightly above, the Fermi energy of the metal. The smallest electric field sufficient to ionize the neon atoms is reached only above atoms protruding from the surface. In pure metals these protruding atoms are usually located in ledge, or kink-site positions (Figure 2) at the edges of different stacks of lattice planes. The edges of one stack of *hkl* planes form almost concentric polygons, or rings, because of the intersection of each stack with the more or less spherically shaped tip surface (Figure 2). This arrangement of atoms with localized high-field regions lead to the well-known crystallographic pattern of FIM micrographs of pure metals and dilute alloys (Figure 3*a*).

In most two-phase alloys the precipitates appear in either bright or dark

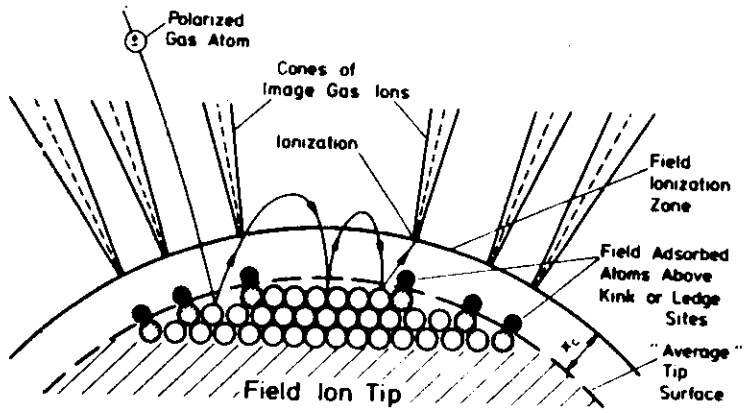

Figure 2 The principle of field-ion image formation: only the hatched atoms are imaged.

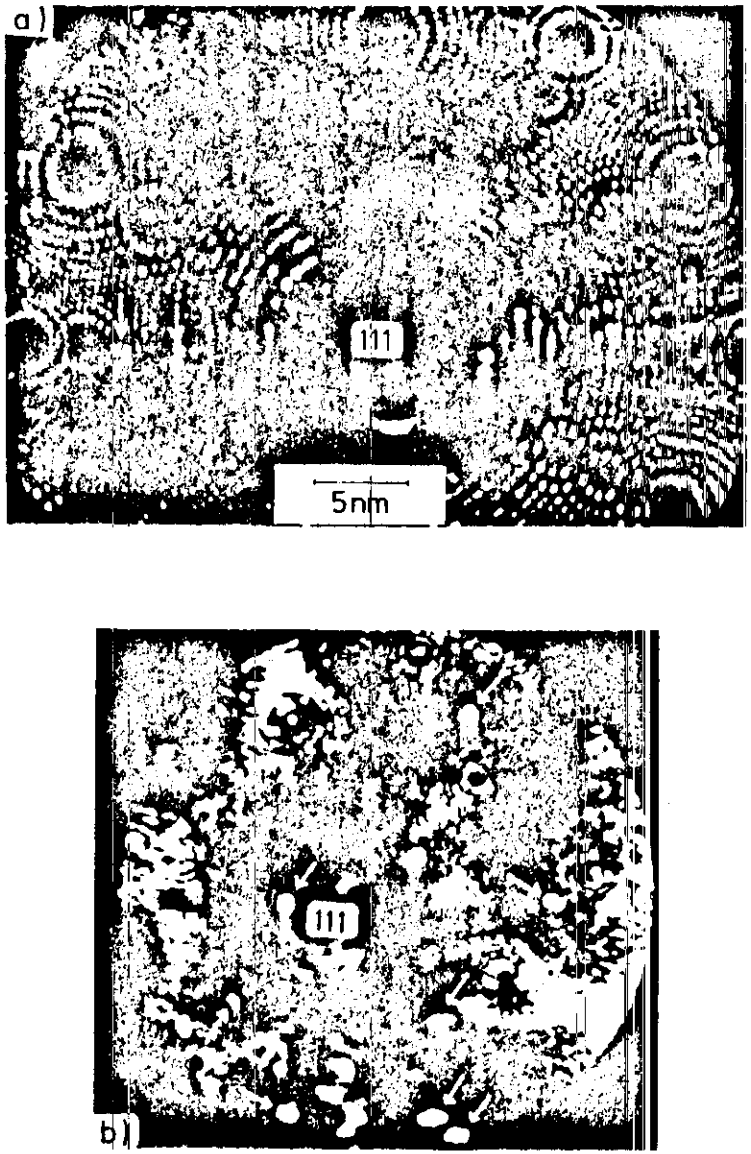

Figure 3 Neon field-ion image of Cu–1 at.% Fe aged for 100 min at 500°C. Arrows indicate nuclei of a metastable iron-rich precipitate phase (*a*). The same alloy after aging for 550 min (*b*). Note the enhanced contrast of the Fe-rich clusters and the reduced resolution of the matrix as compared to (*a*) (25).

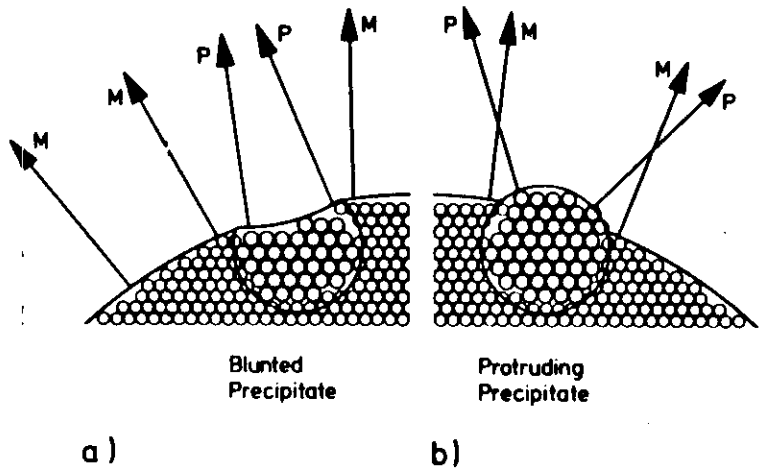

Figure 4 Surface topology around precipitates after the tip reaches a steady-state end-form. (*a*) blunted precipitates appear in dark contrast; (*b*) protruding precipitates appear in bright contrast. Also, the trajectories of field-evaporating ions, originating from the matrix (*M*) or the precipitate (*P*), are shown schematically.

contrast to the surrounding matrix. In both cases, after some field evaporation a steady state end-form of the FIM tip evolves, with the precipitates either protruding from the emitter surface (*i*) or being blunted (*ii*) as compared to the local radius of curvature of the adjacent matrix (Figure 4). These local deviations in the radius of curvature above the precipitates are caused by a respectively higher (*i*) or lower (*ii*) evaporation field than is necessary to field evaporate the surrounding matrix. Although not yet fully understood, it is assumed that the electric field variations associated with variations in surface topology, caused by the precipitate, are responsible for an enhanced (*i*) or reduced (*ii*) ionization probability above the precipitates and, hence, a bright or dark contrast, respectively. Copper-rich precipitates in Fe-Cu show a dark contrast; gold-rich precipitates, which are more resistant to field evaporation than the surrounding matrix, appear bright in Fe-Au imaged with neon (19). However, the contrast of a particular phase can also depend on the image gas and the temperature of the tip. For instance, the Cu-rich particles in an Fe-Cu alloy become bright if imaged with hydrogen instead of neon. Gamma-prime precipitates of the type $(Ni\text{-}Co)_3(Al\text{-}Ti\text{-}Cr)$ in a Ni-based superalloy exhibit bright contrast at a tip temperature of 80 K (Figure 5), whereas hardly any contrast is seen at 30 K (20). On the other hand, no contrast is obtained from $\gamma' Ni_3Al$ particles in a binary Ni–14 at.% Al alloy

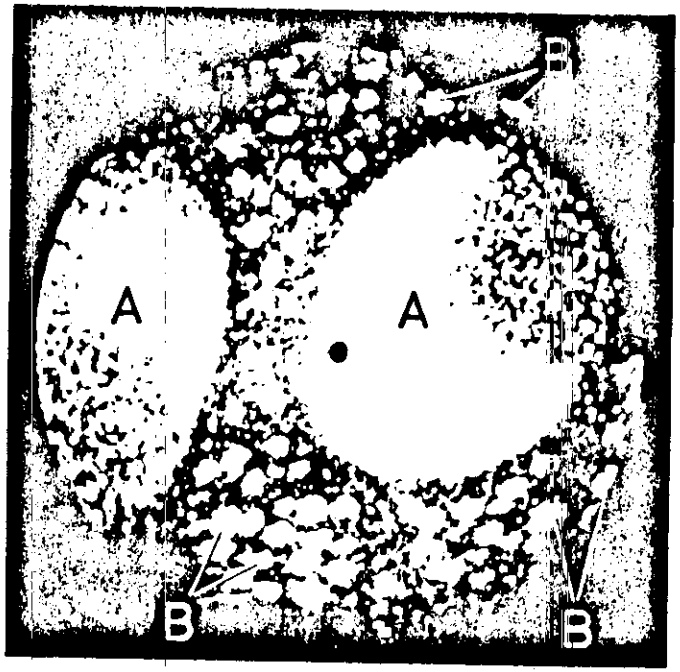

Figure 5 Neon field-ion image of a nickel-based superalloy after a four-stage heat treatment. It exhibits two large (*A*) and many small (*B*) γ′ precipitates (6). (Courtesy P. A. Beaven.)

(21). Apparently, the processes of field ionization and evaporation are highly sensitive to the composition of the precipitates.

FIM images of certain other alloys, e.g. Cu–5 at.% Ti or Co-Ta, aged in the two-phase region of the phase diagram, look similar to those of one-phase materials, and do not reveal any precipitate contrast, despite the evidence of AP analyses and TEM, which have clearly established the presence of second-phase particles. Figure 6*a* shows a rather regular field-ion image of a Cu–5 at.% Ti specimen aged for 6 h at 350°C; no discrete particles are seen. However, after a rupture in part of the tip, suddenly the precipitated phase (dark contrast in Figure 6*b*) can be clearly distinguished from the bright matrix. Following some field evaporation the contrast between the two phases disappears again. These peculiar contrast features are not observed in less concentrated, aged Cu–1.9 at.% Ti where the Cu_4Ti particles always appear in dark contrast, Figure 6*c* (22). Similar changes in the appearance of the phase contrasts have been reported for Co-Ta (23). In aged Co–7.5 at.% Ti no obvious signs of precipitation are visible with fairly

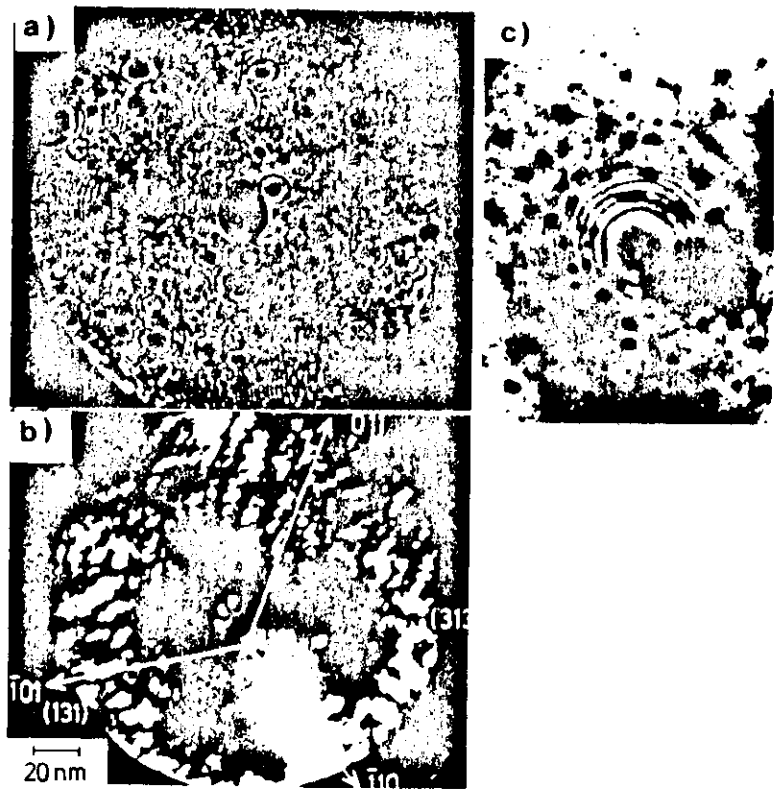

Figure 6 Neon field-ion images of Cu–5 at.% Ti aged for 6 h at 350°C before (*a*) and after (*b*) part of the tip has ruptured. Only in *b* do the two phases appear in contrast. Figure 6*c* shows Cu–1.9 at.% Ti aged for 5 min at 350°C. Cu_4Ti are discernible by their dark contrast (22). (For better reproduction of *c*, the contrast of some Ti-enriched clusters was artificially enhanced.)

sharp tips ($r_t \lesssim 40$ nm) (24). However, after blunting the tips to about 80 nm by continuous field evaporation, the Co_3Ti precipitates become visible.

These examples demonstrate that the absence of any precipitation contrast in the FIM pattern does not necessarily mean that the alloy has not yet decomposed into two distinct phases. In alloys where the precipitated phase is not visible, one must rely on atom-probe analysis (following section) to investigate the state of phase separation.

The contrast features of field-ion images of decomposing alloys also frequently depend on the degree of decomposition. This is shown in Figures 3*a* and 3*b* for a Cu–1 at.% Fe alloy (25). After aging the alloy for 100 min at

500°C, the matrix is still atomically resolved, and the contrast of the precipitates is rather faint (*a*). After aging for 150 min, the atomic resolution of the matrix atoms (Cu) is lost, but the contrast of the precipitates is strongly enhanced (*b*). The contrast enhancement in later stages of the precipitation reaction, at the expense of image resolution of the matrix, has been observed quite frequently in various two-phase alloys.

Because of the localized change in the radius of curvature above precipitates (Figure 4), a considerable unknown change in the magnification (M) of the particular precipitate results (Equation 1). If the precipitates are nonspherical, e.g. thin platelets or γ' zones, the magnification can even be rather anisotropic. Therefore, it is generally not possible to determine the size of (visible) particles directly from an FIM micrograph just by using the average magnification ($\bar{M}$, Equation 1).

Nevertheless, the size and morphology of visible precipitates can often be determined very accurately without knowing M by using the *persistence-size* technique (Figure 7*a*). By controlled field evaporation several lattice planes of a previously identified pole (hkl) are successively removed. Whenever a precipitate becomes visible in the vicinity of this pole, the number of planes (n_{hkl}) that have to be evaporated between the appearance and disappearance of the particle are counted. The dimension of the precipitate along the (hkl) direction is then immediately obtained as $d(hkl) \times n_{hkl}$, with a depth resolution of ~ 0.2 nm. By recording the variations in intersectional area of the precipitate with the tip surface during the dissection of the precipitate, its morphology can be determined in detail.

1.3 *Atom-Probe Analyses*

The chemical identification of a single ion is achieved by first measuring its time of flight (t), and subsequently evaluating its mass-to-charge ratio (m/n) (Figure 1). For this purpose the atoms are field evaporated at a well-defined instant by superposing a high-voltage pulse of a few nanoseconds rise-time onto the tip, which is held at the imaging voltage (V_{DC}) (pulse field evaporation). A pulse width of about 15 nsec and a pulse amplitude (V_P) of about 0.15 V_{DC} are found to be appropriate for the analysis of most alloys. Due to the sharp drop in field strength within a few nm above the tip surface, the field-evaporated ions reach their terminal velocity (v) shortly after the desorption event. The ions then drift with an energy

$$n \times e(V_{DC} + V_P) = \tfrac{1}{2}mv^2 = \tfrac{1}{2}m\frac{d^2}{t^2}, \qquad (2)$$

over a distance (d) virtually equal to the tip-to-detector distance (Figure 1). After a time-of-flight t, they strike the ion-detector. In essence, Equation (2)

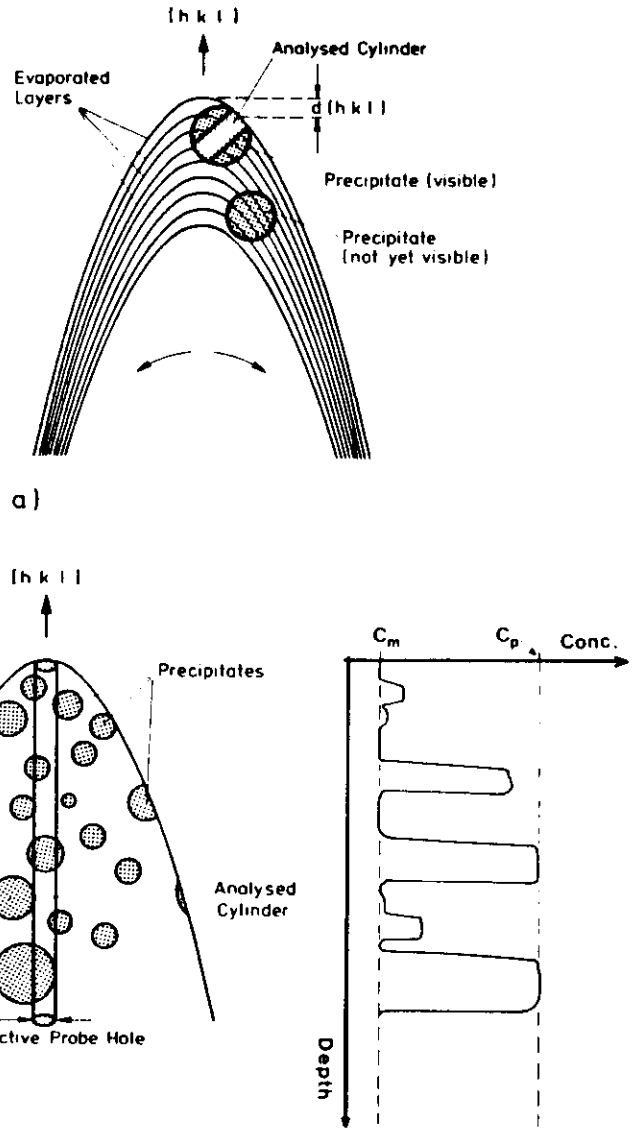

Figure 7 (*a*) "Persistence-size" technique for the accurate determination of the size and morphology of visible precipitates. The principle of selected area AP analysis of a visible precipitate is also illustrated. In (*b*), the nearly cylindrical volume analyzed during a "random-area" AP analysis, and the resulting composition profile are shown. Only some particles are completely cut by the cylinder.

already contains all measurable quantities for the evaluation of m/n; however, in practice, electronic delay times, pulse shape factors, etc (7) have to be taken into account in order to operate the AP at its optimum mass resolution. For most instruments the latter is of the order $\Delta m/m \approx 1/150$, but can be improved significantly (to about 1/1000) by employing an *energy focusing* ToF spectrometer (26) rather than a conventional one.

In principle, the quantitative microanalysis of decomposing alloys using the atom-probe can be performed in two different ways. The first of these is *selected area analysis* (Figure 7*a*). This type of analysis of the composition of individual particles is confined to precipitates that are discernible in the FIM image. By rotation of the FIM specimen, the particular precipitate is imaged over the probe-hole in the FIM screen. If the effective probe-hole (diameter d_{ap}) is larger than the particle, d_{ap} is decreased by increasing the magnification until the precipitate covers the probe-hole entirely. The composition of the precipitate is then determined by collecting the atoms originating from a cylinder of diameter d_{ap}, and of a length limited by the total depth that can be probed before the precipitate has been completely field evaporated (Figure 7*a*). By continuing to probe into the adjacent matrix to determine the composition of each successively removed lattice plane, the concentration profile across interphase boundaries can also be obtained. As discussed in the previous section, with this method the size and detailed morphology can be determined rather precisely. The accuracy of this compositional analysis depends on the total number of atoms that can be collected from the precipitate. For small particle sizes, such as occur in early precipitation stages, several particles have to be analyzed in order to keep the confidence limits narrow. This requires a sufficient number density of particles, e.g. $\gtrsim 10^{17}$ cm^{-3}.

The second technique is *random-area analysis* (Figure 7*b*). In order to analyze the composition and distribution of particles that are not visible in the FIM, or to obtain information about solute fluctuations in alloys (e.g. spinodally decomposing alloys), it is necessary to determine the concentration profile in a cylinder of considerable length. The cylinder should be more than 100 nm long in one direction ($h'k'l'$), with a sufficient depth resolution (Figure 7*b*). For this purpose, the planar concentration of each successively field-evaporated $h'k'l'$-lattice plane is determined and plotted against the number of evaporated planes. Hence, the depth resolution is equal to the interplanar spacing $d(h'k'l')$. Whenever the analyzed cylinder cuts completely through a particle (Figure 7*b*), its composition and the solute variation across its interphase boundary can be determined directly from the concentration profile. However, if the particle is partly cut by the analyzed cylinder (Figure 7*b*), the concentration profile reveals only a local increase in the solute content as compared to the surrounding matrix (c_m).

but does not give any information about the true composition of the particle (c_p).

Figure 8*a* shows the composition profile along [111] of an aged Cu–2.7 at.% Ti alloy that contains isolated β' Cu_4Ti precipitates. Three particles (*A*) are completely cut, and two are probably only partly cut (*B*) by the analyzed cylinder ($d_{ap} \approx 2.5$ nm). The considerable statistical noise superposed on the actual composition profile results chiefly from the limited number (N) of atoms that can be collected per field-evaporated plane. For $d_{ap} \approx 2.5$ nm, N typically fluctuates between 50 and 120. If ultimate depth resolution of one interplanar spacing is not required, e.g. for slowly varying composition profiles, smoothing of the measured composition profiles can be achieved by summing up the atoms from several successively field-evaporated planes. Small solute clusters that were not unambiguously discernible in the original, blurred AP composition profile can often be deconvoluted through a moving-average analysis; this is another smoothing technique (7). These smoothing procedures, in fact, remove the high frequency components of the original AP composition profile, but also flatten the concentration profiles across interphase boundaries. Therefore, prior to applying any smoothing procedures, the original composition profile, recorded with ultimate depth resolution but rather poor statistics, must be carefully inspected.

By analogy with the analysis-of-time series, the data contained in an AP composition profile are often analyzed in terms of an autocorrelation analysis, provided the distance probed through the specimen is sufficiently large. This statistical analysis furnishes most decomposition parameters that are required for a comparison with theoretical predictions (see following section). During the early stages of phase separation when cluster sizes are small and their number densities large this method is especially useful. Figure 8*b* shows the autocorrelation coefficient $R(k)$ for the concentration profile displayed in Figure 8*a*. $R(k)$ is given by

$$R(k) = \frac{n}{n-k} \frac{\sum_{i=1}^{n-k} (c_i - c_0)(c_{i+k} - c_0)}{\sum_{i=1}^{n} (c_i - c_0)^2}, \qquad 3.$$

where c_i is the concentration of the i-th field-evaporated plane ($h'k'l'$), c_0 the mean concentration, n the total number of field-evaporated planes, and k is the correlation length in units of the interplanar distance $d(h'k'l')$. From computer-simulated atom-probe analyses for which various precipitate microstructures were assumed, it has been established that the parameters k_0, k_1, R_{max}, and R_{min} (Figure 8*b*) are unequivocally related to the mean

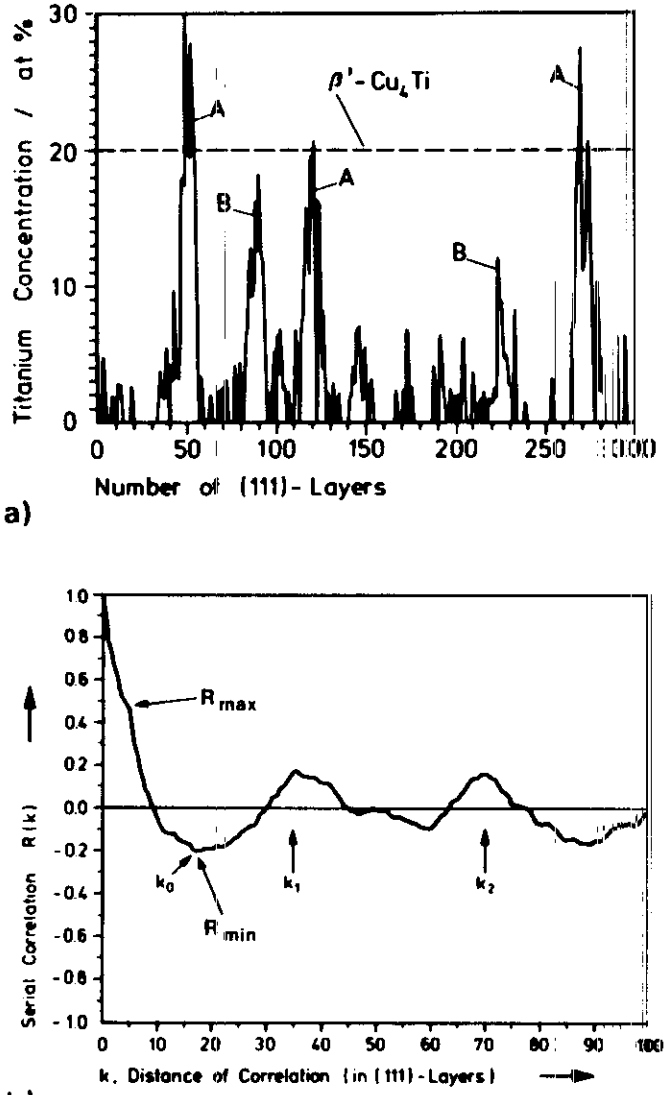

Figure 8 (*a*) Concentration profile along [111] of a Cu–2.7 at.% Ti specimen aged for 500 min at 350°C. On the average, 50 atoms per field-evaporated (111) plane were collected. One removed (111)-layer corresponds to a probing depth of 0.18 nm. Particles completely or only partly cut by the analyzed cylinder are denoted by *A* and *B*, respectively. (*b*) Corresponding correlogram (28).

particle diameter ($2 \times \bar{R}$), the interparticle distance (λ), the particle composition (c_p), and the precipitate volume fraction (f), respectively (27). In particular, computer-simulations yielded $\lambda = k_1 \times d(h'k'l')$, and $2\bar{R} = k_0 \times d(h'k'l')$ for larger particles (e.g. $\bar{R} \gtrsim 1.2$ nm). For size distributions with even smaller mean radii, autocorrelation analyses yield $\bar{R}$ values somewhat larger than the true ones. In Figure 8*b*, the occurrence of the second peak at k_2 is at exactly twice the distance of the first peak, indicating that Cu_4Ti particles are quasiperiodically distributed (28). For randomly distributed, solute-rich clusters of small number density $R(k)$ remains zero for $k > k_0$.

The true composition of a solute-rich cluster is only displayed in a composition profile if the cluster is *completely* covered by the probe-hole (see Figure 7*b*); this requires $d_{ap} < 2\bar{R}$. Although in principle d_{ap} can be made as small as one atomic diameter, reliable statistics require that a certain number of atoms be recorded, hence d_{ap} is on the order of ~ 2 nm. Therefore, in most real analyses of composition fluctuations, the lateral spatial resolution is confined to ~ 2 nm (7).

It is worth noting that both $\bar{R}$ and λ can be obtained from autocorrelation analyses regardless of whether the ratio $d_{ap}/2\bar{R}$ is larger or smaller than unity. Also, the Fourier transform of the autocorrelation factor $R(k)$ yields the (one-dimensional) structure factor $S(\mathbf{q})$ obtained from scattering experiments ($\mathbf{q}$ is a wave vector). Thus, in principle, a random-area AP analysis furnishes all the information about the state of decomposition that can be inferred from $S(\mathbf{q}, t)$, as determined in a SAXS or SANS scattering experiment.

2. RESULTS ON VARIOUS ALLOYS

2.1 *Modes of Decomposition*

As indicated in the previous section, the AP is particularly suited to the study of the decomposition of alloys on a very fine scale. In order to slow down the kinetics to an observable rate, these materials are usually quenched deep into the two-phase field, and the correspondingly large supersaturations then create second-phase nuclei typically 2 nm in diameter. As applied so far, this is below the resolution of conventional transmission electron microscopy. Neutron and X-ray small angle scattering(SAS) are, on the other hand, well suited to the observation of such small particles. For a comparison of the three methods, as applied to the decomposition of alloys, see the proceedings of a recent topical conference (29). The problem with SAS is that it does not reveal the composition of the particles formed, but only their sizes and number density. This is a distinctive feature that differentiates the two modes of *homogeneous*

decomposition (the only type of decomposition reviewed here). The two modes of homogeneous decomposition are detailed below.

In the *nucleation and growth* mode (NG), small particles that differ greatly from the composition of the matrix form by thermal fluctuations, and then grow in size. They are surrounded by a depletion zone in whose concentration gradient the solute diffuses "downhill" to the particle and makes it grow. The other mode, *spinodal decomposition* (SD), involves long-range composition modulations, often periodic ones, that enlarge in amplitude with time, and also somewhat in wavelength, until the final second-phase composition, as prescribed by the phase diagram, or a metastable phase is reached. The solute diffuses "uphill" in the concentration gradient in this case.

The second-phase particle distribution will be the same in the later stages according to both decomposition modes: A distribution of final-composition particles that is often periodic. In NG the solute depletion around particles enforces, along with other factors, finite particle spacings. Thus, a typical scattering experiment does not indicate whether the mechanism of particle formation was NG or SD. It is the initial particle composition, and only this feature (7), that differentiates the two.

It is well known that in the central part of a two-phase field the thermodynamic factor and, accordingly, the chemical diffusion coefficient become negative, which encourages SD. In the peripheral regions close to the solvus, NG decomposition is necessary. The two regions are separated by the spinodal curve, whose definition and practical existence has been doubted in recent times (12). The theoretical spinodal position also depends on the strain energy accompanying the decomposition; it moves to lower T at large misfit strains. The kinetics of both decomposition modes have been studied by AP. The theories explaining these kinetics are summarized next.

2.2 *Theories of NG Kinetics*

According to the classic Becker-Vollmer theory (30), the formation of a coherent second-phase (β) nucleus in a homogeneous matrix (α), involving no size misfit, necessitates the formation of an interface of specific energy $\sigma_{\alpha\beta} > 0$, as well as a gain in chemical free energy (Δf_v) per unit volume of β. For a sphere of radius R, those two terms depend on different powers of R, therefore a barrier must be overcome, which defines a critical nucleus of size

$$R^* = \frac{2\sigma_{\alpha\beta}}{\Delta f_v}, \quad \text{and of extra free energy} \quad \Delta F^* = \frac{16\pi\sigma_{\alpha\beta}^3}{3\Delta f_v^2}. \qquad 4.$$

This energy is supplied by thermal fluctuations with a stationary rate per

unit volume of

$$I_\infty = DN \frac{N_2}{N_3}\left(\frac{\Delta F^*}{3\pi kT}\right)^{1/2} \exp\left(-\frac{\Delta F^*}{kT}\right). \qquad 5.$$

Here D is the solute diffusion coefficient in the matrix, N the atom number density, and N_2 and N_3 are the atomic numbers in the surface and volume of the critical nucleus, respectively. This nucleation rate builds exponentially to the value I_∞, with a time constant τ at least equal to the time needed for the B atoms to diffuse together, i.e. $\tau \geq R^{*2} \times 2/D$.

Once the nucleus is over the critical size it grows from its own matrix environment with a rate given by $R \approx \sqrt{Dt}$ (31). This rate holds for a short period, until the depletion spheres of neighboring particles overlap. Then competitive "Umlösung" (Ostwald ripening) starts, as described in its asymptotic limit ($t \to \infty$), by the classical Lifshiz-Slyozow-Wagner (LSW) theory (32, 33). Accordingly, the mean radius of the size distribution grows as

$$\frac{dR^3}{dt} = b = \text{const}, \qquad 6.$$

while the supersaturation ΔC (assumed to already be small) decreases as

$$\Delta C = (\kappa t)^{-1/3}. \qquad 7.$$

In principle, from the constants b and κ the two parameters of the coarsening kinetics, D and σ, can be evaluated. However, in the range of validity of the LSW theory ($\Delta C \to 0$), ΔC is too small to be measured reliably with the AP or any other technique. Hence, frequently only the product $D\sigma$ can be determined from b.

In practice, the nucleation period is not clearly separated from the coarsening period, so that attempts have been made to describe both processes in a unified theory (8, 9). The number density (N_v) of particles generally changes with time by nucleation, and simultaneously by dissolution due to a changing critical radius. Thus,

$$\frac{dN_v}{dt} = I(t) - N(R = R^*, t)\frac{dR^*}{dt}, \qquad 8.$$

where $N(R, t)$ is the size distribution of the particles. The mean particle radius,

$$\bar{R} = \frac{1}{N_v}\int_{R^*}^{\infty} N(R) R \, dR,$$

changes as

$$\frac{d\bar{R}}{dt} = v(R) + \frac{1}{N_v} I[R^*(t)](R^* - \bar{R}) + (\bar{R} - R^*)\frac{N(R^*)}{N_v}\frac{dR^*}{dt},$$

with

$$v(R) = \frac{D}{\bar{R}}\frac{\bar{c}(t) - C_R}{C_\beta - C_R} \qquad 9.$$

accounting for diffusive growth or dissolution.

The solute concentrations in the matrix and the particle are c and C_β, respectively. C_R is the concentration directly over a particle of radius R, according to Gibbs-Thomson

$$C_R = C_\infty \exp\left(\frac{2\Omega\sigma}{RkT}\right), \qquad 10.$$

where Ω is atomic volume, and C_∞ represents the equilibrium solubility.

Together with the continuity equation, the equations of motion for N_v and R (Equations 8 and 9) have been solved numerically (8, 9) under certain assumptions, in particular those concerning the long-term coarsening behavior, the particle size distribution, and the constancy of D and σ.

A priori, it is not possible to assess the influence of these assumptions on the precipitation kinetics results. Therefore, an algorithm (or "numerical model") has recently been devised (9) that describes the entire course of precipitation within the framework of existing nucleation and growth theories. No simplifying assumptions enter this algorithm; in particular it allows the time evolution of $N(R,t)$ to also be computed. A comparison with experimental results is given later.

2.3 *Theories of SD Kinetics*

Cahn's theory of SD kinetics (10) is conceptually much simpler than that of NG, as it basically involves only diffusion, though uphill, and contains no further stochastic element. [Subsequently, Cook (34) has added a thermal fluctuation term to the theory.] Cahn starts with Fick's law (in one dimension)

$$\frac{\partial c}{\partial t} = \tilde{D}\frac{\partial^2 c}{\partial x^2} = D\left[\frac{c(1-c)}{kT}\frac{\partial^2 F}{\partial c^2}\right]\frac{\partial^2 c}{\partial x^2}. \qquad 11.$$

Here in the thermodynamic factor $[\ldots]$ for F, the so-called gradient-energy density $k(dc/dx)^2$ has to be included to account for the high price of very short wave concentration modulations. This leads, in the linearized form of Cahn's theory (considering the coefficients in Equation 11 to be constant),

to a term $\partial^4 c/\partial x^4$ in Equation 11. Beginning the solution with a Fourier ansatz, certain components will grow exponentially and determine the positions of the evolving precipitates in three dimensions. This growth law is rarely observed; instead, a much slower power law growth, and a slow increase of the dominant wavelengths with time are seen. This fits the pattern predicted by later nonlinear, though numerical, theories (11, 12). Another matter of debate is the behavior of the system as it approaches the spinodal ($\partial^2 F/\partial c^2 = 0$) from either side (29).

2.4 *AP Studies of Decomposition by NG*

After the pioneering papers of Goodman et al (35) on FeCu, quite a number of quantitative studies have been made available.

2.4.1 Ni-Al An alloy of Ni–14 at.% Al decomposes at 823 K, and forms γ' Ni_3Al precipitates coherently with the fcc γ matrix (21). The particles are not directly visible in the FIM (Section 1), but are only discernible in the recorded AP composition profiles (e.g. Figure 8). These particles have been analyzed by the statistical method of autocorrelation, together with computer simulation (Section 1), to yield $\bar{R}$ and the precipitated volume fraction f or N_v. As there are relatively few particles in the analyzed volume, it is difficult to get the particle size spectrum $N(R)$ directly. The solute concentration (C_β) of particles having diameters smaller than the probe-hole size (i.e. $2\bar{R} \leq 2.5$ nm) could not be determined directly from the composition profiles, but also had to be inferred from joint autocorrelation and computer simulation analyses.

One of the most important results is that even the smallest observed precipitates, of radius 10 Å or smaller, have the equilibrium composition Ni–23 at.% Al. This suggests an NG, not an SD character, as has previously been claimed (36). It is interesting to note that at the shortest observed aging times the activation barrier ($\Delta F^* \approx 4kT$) is relatively small. The thermochemistry of the system is sufficiently known to evaluate Δf_v as a function of supersaturation. Also, σ has been measured from overaging kinetics of larger particles, thus R^* can be calculated as a function of the directly measured $\Delta C(t)$, and compared with the AP results on $\bar{R}(t)$. The data obtained at 550°C are shown in Figure 9; they prove that nuclei have been observed. This appears to be the first such observation for a solid-solid diffusive phase transformation.

Figure 10 shows the aging time evolution of the particle density, compared with the one expected from time integration of the nucleation rate. It is evident that there is no pure nucleation stage, but that Ostwald ripening intervenes after a short aging time. Therefore, the unified theories discussed in Section 2.2 are needed to interpret the experimental data.

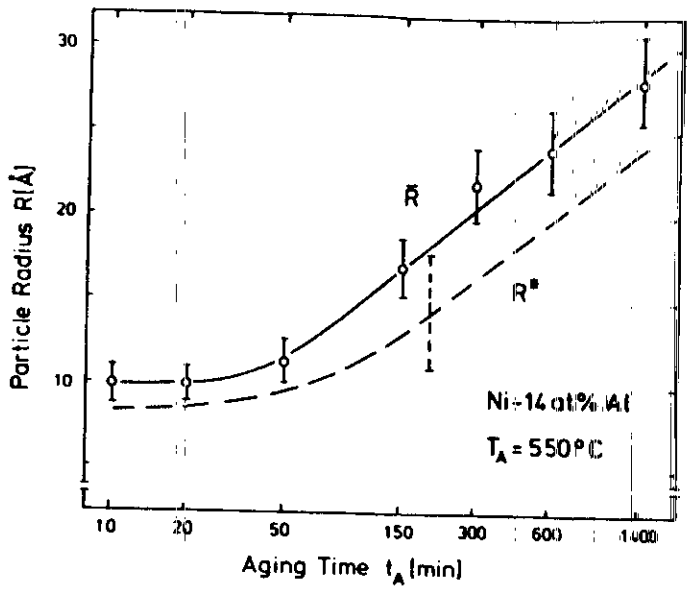

Figure 9 Measured mean particle radius and calculated radius of critical nuclei versus aging time (21).

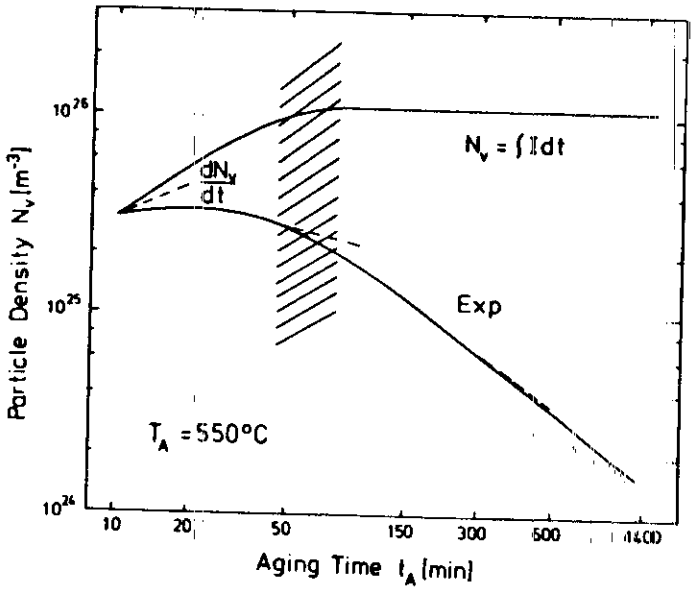

Figure 10 Experimental number density of particles in Ni-14 at.% Al, and calculated density of nucleated particles versus aging time (21).

Figure 11 shows $\bar{R}(t)$ and $R^*(t)$ calculated according to the Langer-Schwartz theory (8), modified to apply far from the critical point (9). The modified theory (MLS theory) uses the nonlinear version of the Gibbs-Thomson equation, and accounts for an incubation time in the nucleation rate (9). Also shown are the results from the "numerical model" (9), which allows the kinetics to be computed more accurately from the precise knowledge of $N(R, t)$, at each stage of the phase transformation. By fitting the theoretical curves to the experimental data, both σ and D can be determined rather accurately. Interestingly, the initial plateau in $\bar{R}(t)$ shows up more strongly in the experiments than in the "numerical model." This probably indicates a limit on the minimum observable particle size in the statistical analysis of AP concentration profiles.

Experimental and theoretical results for the time (τ_h) needed to complete half of the decomposition reaction, i.e. reduce ΔC to half its initial value, are shown in Figure 12. At the high (relative) supersaturation (y_0) used here, τ_h is the time needed to overcome resolutioning effects caused by overaging rather than by nucleation itself, which dominates at small y_0. In addition, an evaluation of the incubation time of nucleation (9) indicates that clusters of Al atoms diffuse together and disperse again several (c_w) times before a critical nucleus is formed.

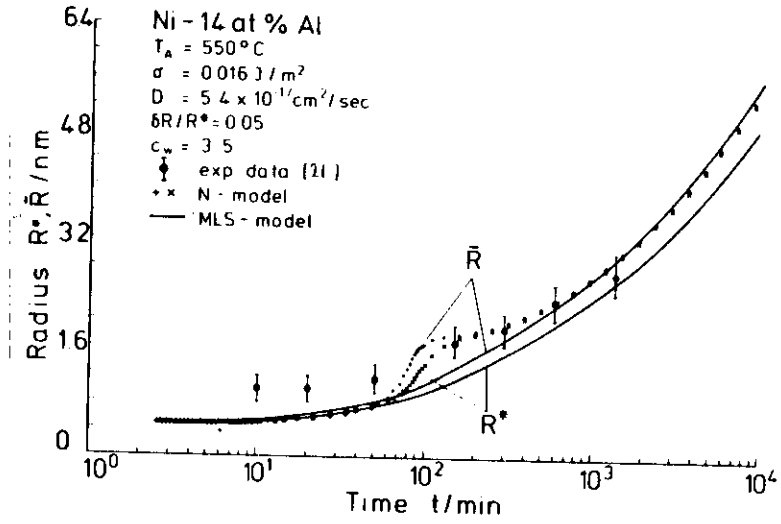

Figure 11 Fit of numerical model (9) and modified Langer-Schwartz model (8) to mean particle radius $\bar{R}$ versus aging time in Ni-14 at.% Al (21). R^* = calculated radius of nuclei. For other parameters see text.

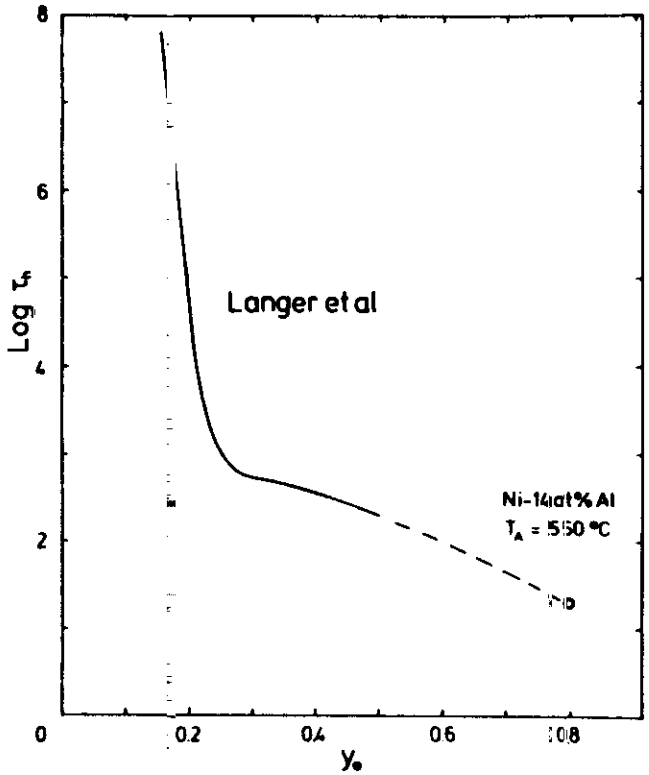

Figure 12 Half-time of decomposition versus normalized supersaturation according to theory (8) and experiment (11).

2.4.2 Ni-Cu-Al The Ni 36% Cu 9% Al alloy (37) is interesting because in the ternary various nonconodal paths of decomposition are possible in principle, and the third component may enrich the particle interface. Again, there is very little misfit between the γ' precipitate and the fcc α matrix. In this alloy FIM does image the two phases in different contrast (Section 1, Figure 13), so particle diameters can be measured more directly, and compared with those analyzed from concentration profiles. Particles of the equilibrium composition $(Ni_{.8}Cu_{.2})_3Al$, at 580°C, are found at the very earliest aging times.

Of particular interest is the composition profile across a particle interface, as measured by AP (Figure 14). The composition changes very sharply at the interface (within three lattice planes); this is expected thermodynamically for the relatively low aging temperature. Becker's

Figure 13 FIM image of decomposed Ni 36 at.% Cu 9 at.% Al after aging for 420 min at 580°C (37).

nearest-neighbor interaction model leads one to expect $\sigma = 18$ mJ m^{-2} for Ni-Ni_3Al; the measured value is 16 mJ m^{-2}. For the ternary alloy $\sigma = 52$ mJ m^{-2} is found. The large change upon adding Cu remains mysterious. There is some enrichment of Cu in the (NiCu)/$(NiCu)_3Al$ interface (Figure 15), but this seems to be a nonequilibrium kinetic feature, as Al diffuses faster than Ni and Cu, but the sum of Ni and Cu concentrations remain constant.

Again, the kinetics of nucleation and growth have been studied in detail and compared with the unified theories. In the case of Ni-Cu-Al, some

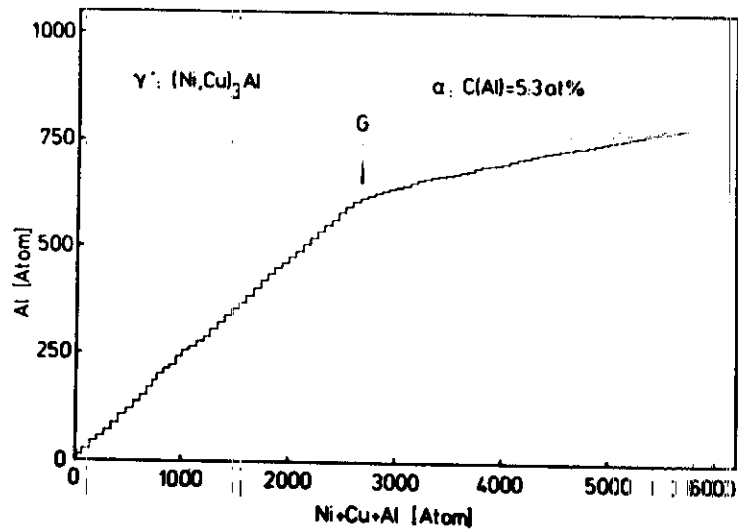

Figure 14 Interface composition profile of precipitate in Ni 36%Cu 9%Al measured as number of field-desorbed Al atoms per total number of atoms (37) in 420 min at 580°C.

particle size distributions have been measured; they are found to be 2-3 times wider than that calculated by LSW (32, 33). In this alloy the work of nucleation, $\Delta F^*/kT = 27$ at 540°C, or 16 at 500°C, is much larger than in Ni-Al. Diffusion coefficients determined from the aging kinetics are on the order 10^{-16} cm^2 s^{-1}, and are not influenced by quenched-in vacancies, which should be annealed out long before the aging times considered here.

One last point of interest is the observed distribution of particle distances. It is a Poisson-type distribution, with a standard deviation of about 60% that of a random distribution; thus showing a tendency toward a regular spacing, as discussed above.

2.4.3 Cu-Fe The hardening of Cu by 1.15% Fe was studied (26) as a function of precipitated volume fraction and particle radius, using FIM measurements. Again, the particles are visible with FIM because of their contrast with the matrix. During aging at 500°C, the particle radius remains constant ($\bar{R} = 0.6$ nm) for the first 150 min while the particle density grows. This behavior appears to be typical for many NG decomposing alloys studied with FIM.

2.4.4 Cu-1.9 at.% Ti Aging of Cu-Ti alloys of Ti contents between 0.5–5 at.%, at $T = 300$–450°C leads to the formation of metastable, ordered, Cu_4Ti precipitates (22, 38). The FIM images of Cu–1.9 at.% Ti aged for only

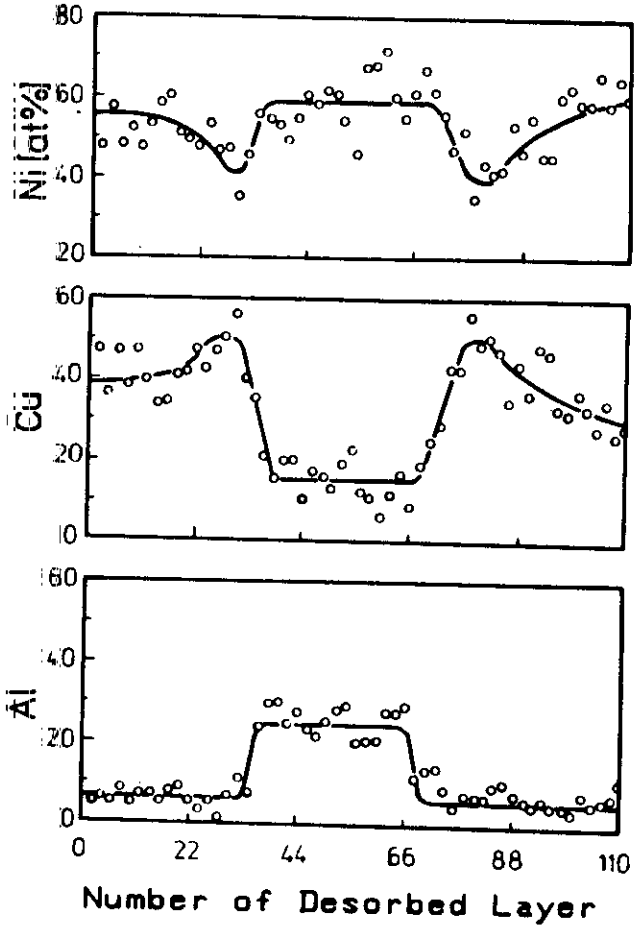

Figure 15 Composition profiles across precipitate in Ni 36 at.% Cu 9 at.% Al.

2.5 min at 380°C reveal many discrete precipitates ($\bar{R} \approx 1$ nm), with sharp interphase boundaries in black contrast (e.g. Figure 6). An extensive FIM and AP analysis of the precipitation kinetics led to the conclusion that at 350°C, Cu–1.9 at.% Ti decomposes via an NG reaction. As shown in Figure 16, the "numerical model" describes the experimental data rather well for $\sigma = 167$ mJ m^{-2}, and $D = 2.5 \times 10^{-15}$ cm^2 s^{-1} (9, 22). The large value of σ, relative to the one in Ni-Ni$_3$Al, and the correspondingly large $\Delta F^* \approx 7kT$ makes for a relatively short nucleation period, nor the stage at which coarsening follows the

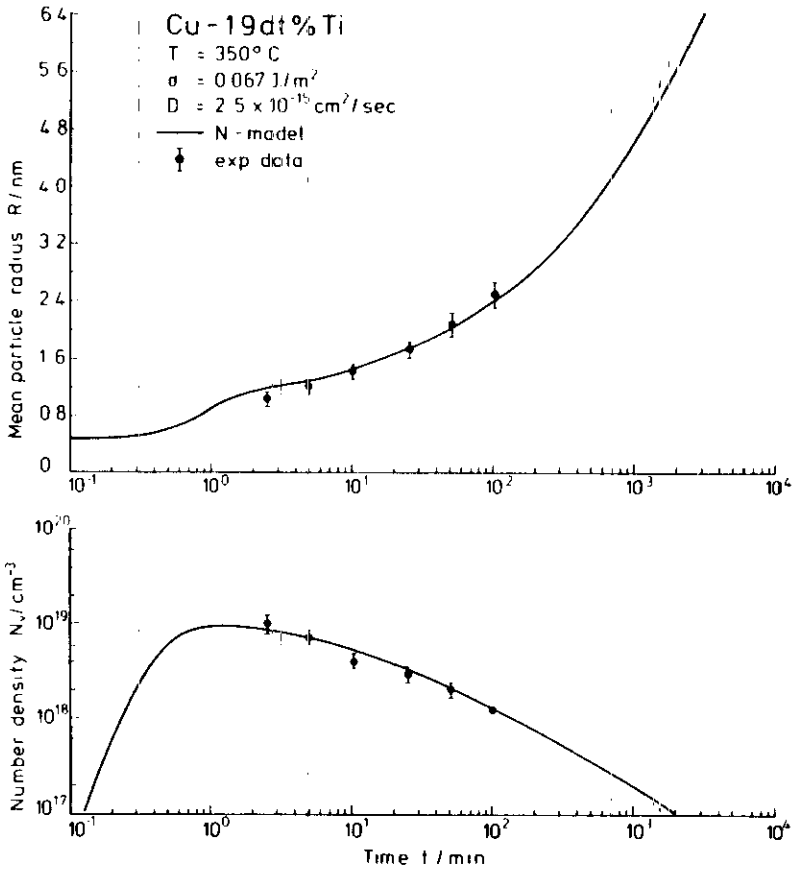

Figure 16 Fit of numerical model to particle radius and particle density versus aging time in Cu–1.9 at.% Ti (22).

LSW kinetics ($t > 10^5$ min), are covered by the experimental period ($2.5 \leq t \leq 10^2$ min) (9).

Because of the relatively large ΔF^* in Cu–1.9 at.% Ti, the nuclei rapidly attain sizes outside the range in which particle growth is dominated by stochastic processes, i.e. $d\bar{R}/dt \gg dR^*/dt$. Theoretically, this situation—relative to that of Ni-Al, where $\bar{R}$ cannot escape from R^*—is advantageous for the unified theories (Section 2.2). These theories face difficulties when nucleation, which they describe as a stochastic process, and growth or redissolution, described in a deterministic way, intervene significantly (9).

It is worth noting that the value for D is larger, by a factor of about 350, than the interdiffusion coefficient obtained by extrapolating the available high temperature data to 350°C. This strongly positive deviation of D at low temperatures from an Arrhenius plot is not presently understood. However, it appears to be typical of alloys undergoing phase separation at low homologous temperatures (22).

2.5 *AP Studies of SD*

2.5.1 Cu-Ti Aging of Cu-Ti alloys of Ti contents between 0.5 and 5 at.%, at $T = 300$–450°C, leads to the formation of ordered Cu_4Ti precipitates. Based on the modulated precipitate microstructure observed in the TEM, it was concluded that decomposition of the more concentrated alloys is continuous, i.e. of the SD type. As stated above, this criterion is not sufficient to exclude a NG mechanism, so AP was used (22, 28, 38) to establish the evolution of Ti concentration amplitude and wavelengths in a number of alloys. Recently, SANS was also applied to these alloys.

Decomposition of Cu–2.7 at.% Ti at 350°C has been studied with the AP FIM (28). Since the second-phase particles were not clearly discernible in the FIM, extended AP composition profiles were recorded and analyzed by statistical models. Aging for 10 min at 350°C led to the formation of small Ti-rich clusters with mean diameters of $2\bar{R} \approx 1.1$ nm, and a mean center-to-center spacing (or mean composition modulation wavelength) of $\lambda \approx 2.8$ nm. $\bar{R}$ and λ grew from the beginning according to $\bar{R} \approx t^{1/4}$, and $\lambda \approx t^{1/3}$ (Figure 17*a*, *b*). For $t < 50$ min, the diameter of the clusters remained smaller than that of the probe-hole used for the AP analyses ($d_{ph} \approx 2.5$ nm). Therefore, the true Ti amplitude of the composition modulations could not be determined directly from the AP composition profiles, but rather had to be inferred from a comparison of the measured profiles with those obtained from computer simulations (22, 28). Using this procedure, the maximum Ti concentration of the clusters appeared to increase continuously (Figure 17*c*) until it reached 20 at.%, as expected for Cu_4Ti after $t \approx 50$ min. (At this stage $d_{ph}/2\bar{R} \approx 1$, thus, the Ti concentration could be determined directly from the composition profiles.) The apparently continuous increase of the Ti concentration of the incipient precipitates can be taken as evidence for an SD reaction. It must be emphasized, however, that the results displayed in Figure 17*c* were derived under the assumption that for $t < 50$ min the composition waves have a sinusoidal form. According to the figure, after 10 min of aging the Ti-enriched clusters ($2\bar{R} \approx 1.1$ nm) contain only about four Ti atoms. This number appears to be too small to be reliably deconvoluted from the composition profiles, which are blurred by statistical noise. Hence, the results shown in Figure 17*c* for $t \leq 25$ min should be regarded with caution.

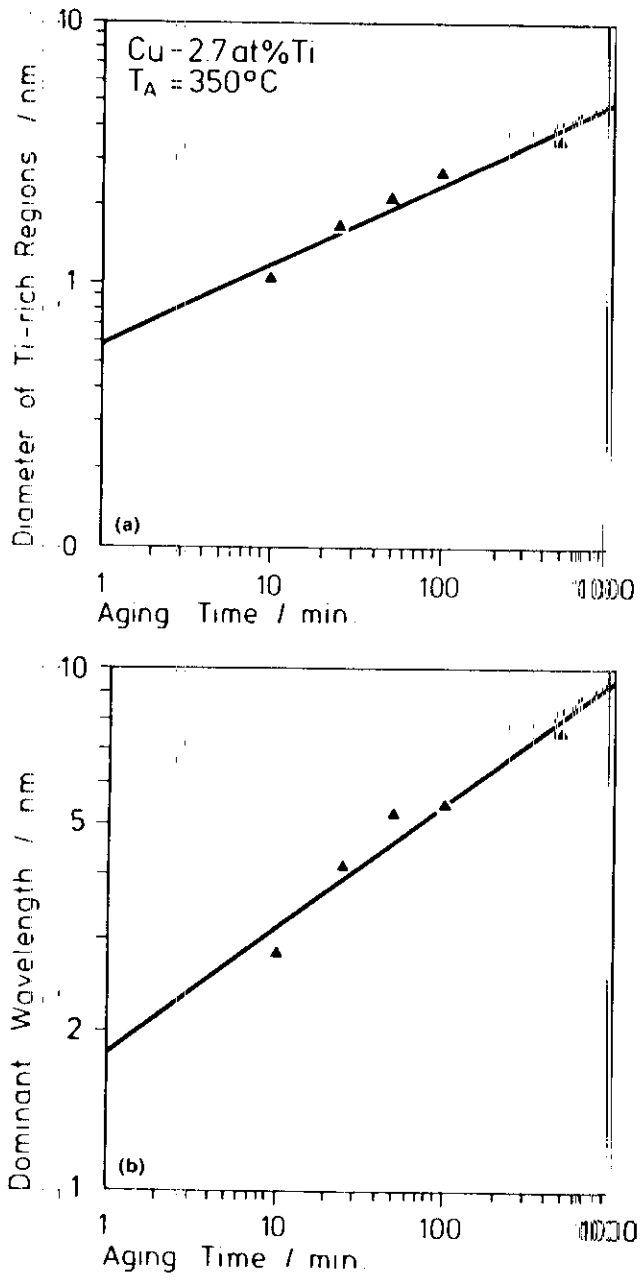

-30-

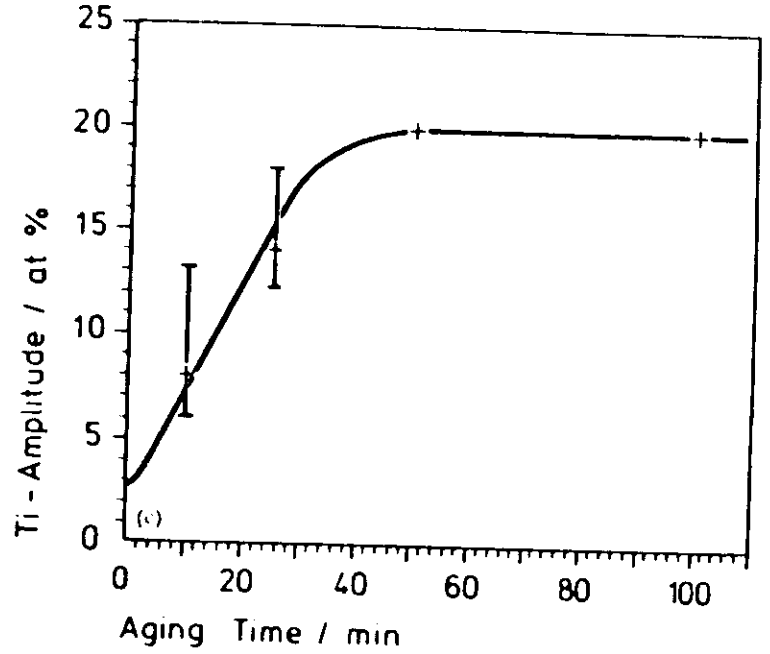

Figure 17 Measured parameters characterizing spinodal microstructure versus aging time at 350°C in Cu–2.7 at.% Ti (28).

2.5.2 Fe-Be In this system a low temperature miscibility gap involves the formation of an ordered Fe-Be phase (B2) from a bcc iron-rich solid solution. The Fe–25 at.% Be alloy studied in the FIM (39) was aged at 350°C. It shows a beautiful macrolattice of brightly imaged, isolated, cubical, iron-rich particles, aligned along ⟨100⟩, in agreement with TEM observations (Figure 18). The microstructure coarsens according to a time law $d^n - d_0^n = kt$, $n = 2, \ldots, 3$. The decomposition is likely to be of the SD type, although the regular array of iron-rich particles could also be the result of the considerable misfit strain involved (~4%).

2.5.3 Fe-Cr-Co Alloys of Fe 28% Cr 15% Co, with minor additions of 1% Al, and 0.25% Zr, are useful as ductile permanent magnets (CHROMINDUR). They derive from the Fe-Cr phase diagram, which decomposes into two bcc phases (called α_1 and α_2) if the σ phase is suppressed (especially by the Co addition). The Co also extends the miscibility gap to a higher temperature, and makes it asymmetric toward the Fe side. The aging cycle used in optimum permanent magnet

-31-

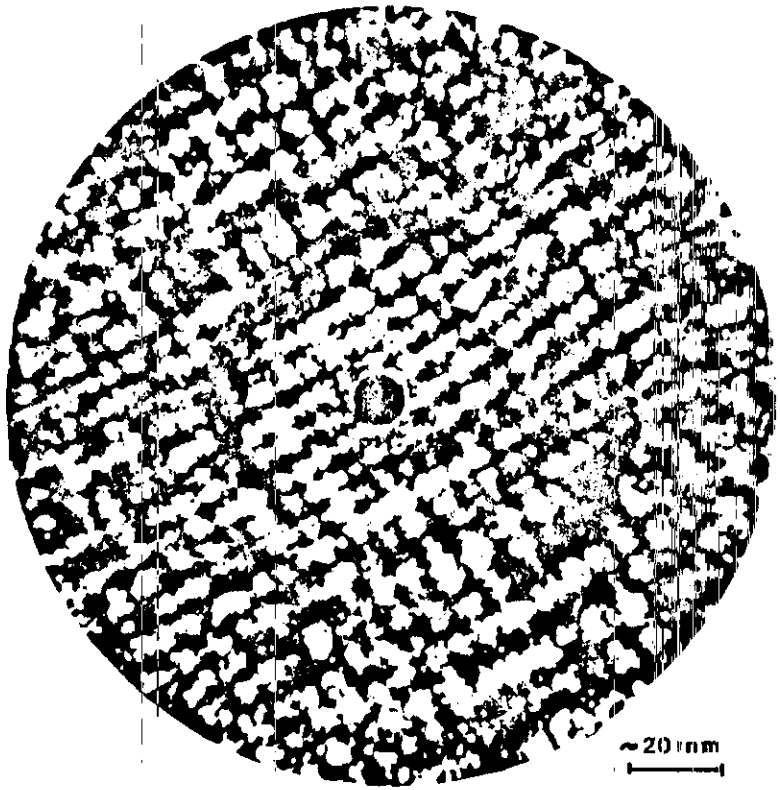

Figure 18 Neon FIM image of Fe 25% Be aged for 2 h at 350°C. (Courtesy S. S. Brenner, Pittsburgh.) (39).

production [to give the maximum energy product $(BH)_{max}$] is rather complicated. It involves aging in a magnetic field just below the Curie temperature, and critical temperature of the gap, i.e. at 625°C, and further aging at 525°C, to increase the concentration amplitudes. The resulting microstructure of the optimum magnet is shown in Figure 19 (40, 41). The Fe-rich phase images brightly, the Cr-rich phase darkly.

As one field evaporates the tip of the sample in the AP, one follows the contiguity of the two phases in depth. Both phases are sponge-like, interconnected, and do not resemble iron-rich ellipsoids in a chromium-rich matrix, as assumed in the elongated single-domain (ESD) theory of permanent magnets. In the ESD theory, the magnetization of a ferro-

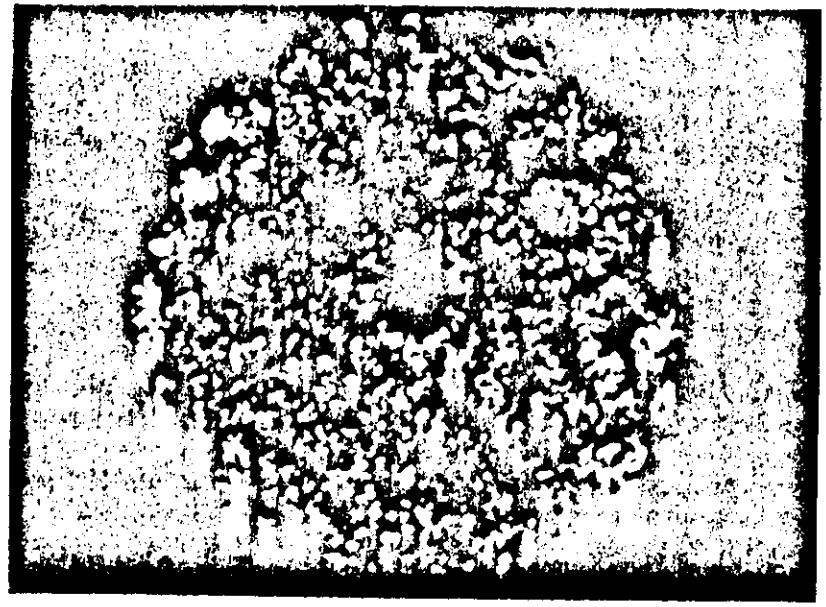

Figure 19 Neon FIM image of CHROMINDUR after aging to optimum magnetic hardness (40).

magnetic phase is fixed to the long axis of the ellipsoid, which is isolated from its neighbors by a paramagnetic matrix. This model also does not apply because *both* phases are ferromagnetic, according to inferences from AP analyses. Figure 20 gives in-depth concentration profiles for Fe, Cr, and Co; the Al seems to follow the Fe, as does the cobalt. It is clear that where Cr enriches, Fe and Co move out. The composition of α_1 is Fe 6% Cr 22% Co, and that of α_2 is Cr 26% Fe 6% Co. The latter composition is, in fact, weakly ferromagnetic at 300 K, with an estimated Curie temperature of 80°C. The volume of α_2 is 40%.

The kinetics of decomposition is followed separately during aging at 600°C or 525°C. As seen in Figure 21, the Cr concentration amplitude in the dark phase changes slowly with time, as expected for SD. The periodicity (λ) and mean thickness of α_2 regions also increase slowly with time, according to a $t^{0.24}$ law. Again, this agrees with nonlinear SD theory. The coercivity of such a microstructure must derive from Bloch wall pinning, the walls find lower energy positions in the dark than in the bright phase. The decomposition of Fe-Cr itself was also studied recently (42). "Alnico" magnets were also investigated by AP FIM (43).

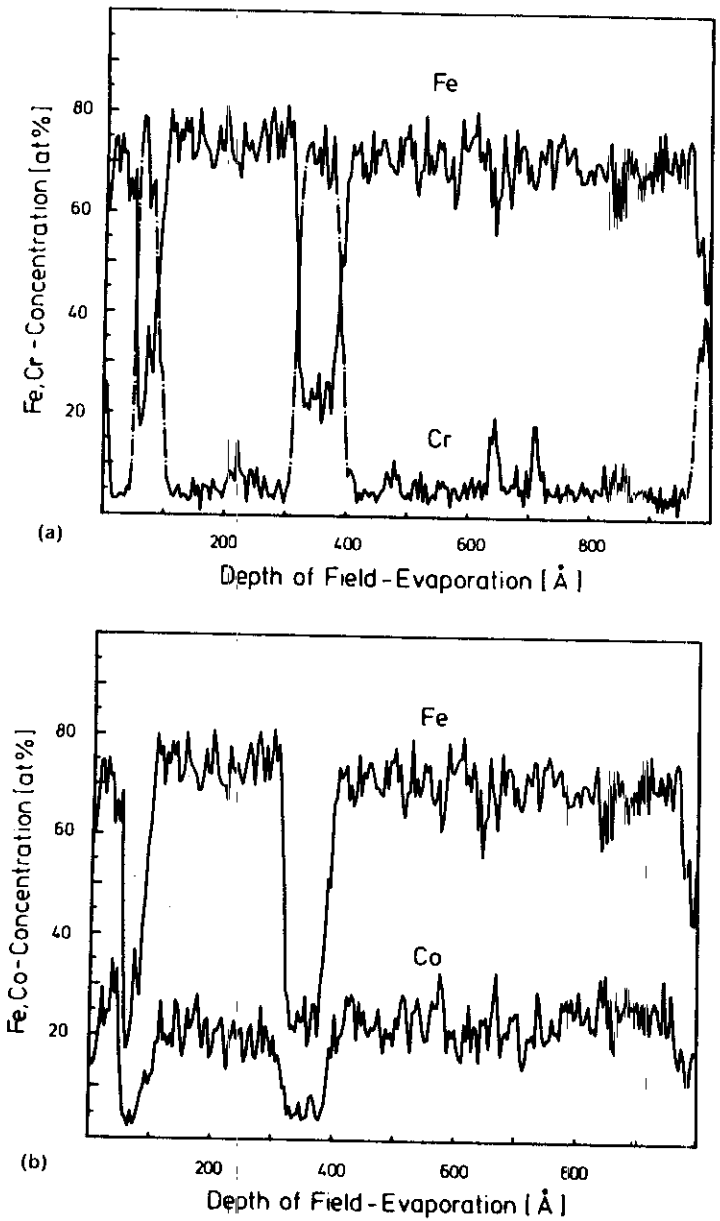

Figure 20 Concentration profiles of CHROMINDUR after aging to optimum magnetic hardness (40). Abscissa is depth of evaporation in nm.

-34-

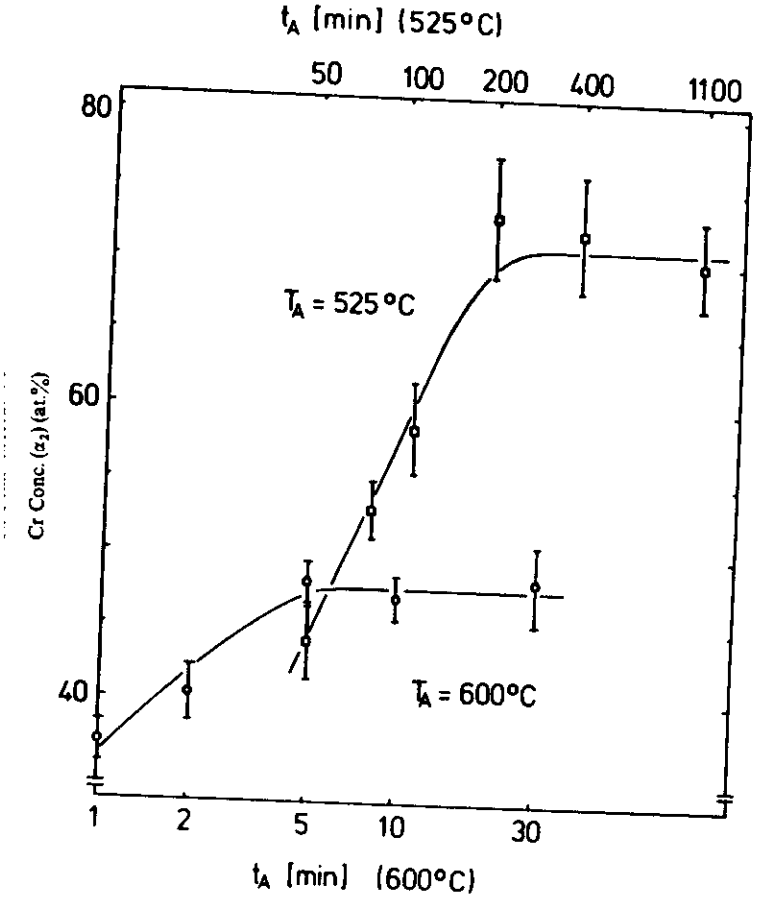

Figure 21 Chromium concentration in dark (α_2) phase of Fe 28 at.% Cr 15 at.% Co 1 at.% Al versus aging time at two temperatures (40).

2.6 *Conclusions*

The above examples of alloy systems whose decomposition has been studied by AP FIM clearly show the extensive interaction between theory and experiment made possible by the new technique. In the case of NG, considerable understanding and agreement have been reached; however, this is still lacking for the spinodal type of decomposition. Here both theoretical and experimental efforts are badly needed.

-35-

ACKNOWLEDGMENT

P. Haasen is grateful to Stanford for its hospitality during the tenure of the Walter Schottky Professorship. Both authors acknowledge the contributions of their colleagues R. Kampmann, H. Wendt, J. Piller, L. von Alvensleben.

Literature Cited

1. Müller, E. W., Panitz, J. A., McLane, S. B. 1968. *Rev. Sci. Instrum.* 39:83
2. Miller, M. K., Smith, G. D. W. 1977. *Met. Sci. J.* 11:249
3. Turner, P. J., Papazian, J. M. 1973. *Met. Sci. J.* 7:81
4. Andrén, H.-O., Henjered, A., Nordén, H. 1980. *J. Mater. Sci.* 15:2365
5. Wagner, R., Brenner, S. S. 1978. *Acta Metall.* 26:157
6. Beaven, P. A., Miller, M. K., Smith, G. D. W. 1977. *Prof. Inst. Phys. Conf. Ser.* 36:199. London: Inst. Physics
7. Wagner, R. 1982. *Field-Ion Microscopy in Materials Science.* In *Crystals: Growth, Properties and Applications*, Vol. 6, pp. 1–116. Berlin: Springer-Verlag
8. Langer, J. S., Schwartz, A. J. 1980. *Phys. Rev. A* 21:948
9. Kampmann, R., Wagner, R. 1984. See Ref. 29, p. 91
10. Cahn, J. W. 1968. *Trans. AIME* 242:166; 1966. *Acta Metall.* 14:1685
11. Langer, J. S., Baron, M., Miller, H. D. 1975. *Phys. Rev. A* 11:1417
12. Binder, K., Billotet, C., Mirold, P. 1978. *Z. Phys.* 30:183
13. Wagner, R. 1981. *Czech. J. Phys B* 21:198
14. Brenner, S. S., McKinney, J. T. 1970. *Surf. Sci.* 23:158
15. Andrén, H.-O., Nordén, H. 1979. *Scand. J. Metall.* 8:147
16. Hall, T. M., Wagner, A., Seidman, D. N. 1977. *J. Phys. E* 10:8384
17. Miller, M. K., Beaven, P. A., Smith, G. D. W. 1979. *Surf. Interface Anal.* 1:149
18. Müller, E. W., Tsong, T. T. 1969. *Field Ion Microscopy*. New York: Elsevier
19. Brenner, S. S., Miller, M. K. 1980. *Proc. Int. Field Emiss. Symp.*, ed. Y. Yashiro, N. Igata. Tokyo: Univ. Tokyo. 238 pp.
20. Beaven, P. A., Delargy, K. M., Miller, M. K., Smith, G. D. W. 1978. *Proc. Int. Congr. Electron Microscopy, Toronto*, 1:626. Ontario: Microscop. Soc. Canada
21. Wendt, H., Haasen, P. 1983. *Acta Metall.* 31:1649
22. von Alvensleben, L., Wagner, R. 1984. See Ref. 29, p. 143
23. Youle, A., Ralph, B. 1972. *J. Micros.* 95:309
24. Davies, D. M., Ralph, B. 1972. *J. Micros.* 96:343
25. Wendt, H., Wagner, R. 1982. *Acta Metall.* 30:1561
26. Müller, E. W., Krishnaswamy, S. V. 1974. *Rev. Sci. Instrum.* 46:1053
27. Piller, J., Wendt, H. 1982. *Proc. 29th Int. Field Emiss. Symp.*, ed. H.-O. Andrén, H. Nordén, p. 265. Stockholm: Almquist & Wiksell
28. Buchl, K.-E., Wagner, R. 1981. *Proc. Int. Conf. Solid-Solid Phase Transf.*, ed. H. I. Aaronson, D. E. Laughlin, R. F. Sekerka, C. M. Wayman. Warrendale, Penn: Met. Soc. AIME, p. 185
29. Haasen, P., Gerold, V., Wagner, R., Ashby, M. F., eds. 1984. *Decomposition of Alloys: The Early Stages, Acta Metall. Scri. Metall. Conf. Series.* Oxford: Pergamon. Vol. 2, pp. 1–239
30. Russell, K. C. 1970. In *Phase Transformations*, 6:219. Metals Park, OH: ASM
31. Ham, F. S. 1958. *J. Phys. Chem. Solids* 6:335
32. Wagner, C. 1961. *Z. Elektrochem.* 65:581
33. Lifshiz, T. M., Slyozow, V. S. 1961. *Phys. Chem. Solids* 19:35
34. Cook, H. E. 1970. *Acta Metall.* 18:297
35. Goodman, R. S., Brenner, S. S., Low, J. R. 1973. *Metall. Trans. A* 4:2363, 2371
36. Hill, S. A., Ralph, R. 1982. *Acta Metall.* 30:2219
37. Liu, Z. G. 1984. *Nachr. Gött. Akad. Wiss.* 2:13; Liu, Z. G., Wagner, R. 1984. *J. Phys. Paris Colloq.* In press
38. von Alvensleben, L., Wagner, R. 1982. See Ref. 27, pp. 563–72
39. Miller, M. K., Brenner, S. S., Burke, M. G., Soffa, W. A. 1984. *Scri. Metall.* 18:111–16
40. Zhu, F., Wendt, H., Haasen, P. 1982. *Scri. Metall.* 16:1175–80
41. Zhu, F., Wendt, H., Haasen, P. 1984. See Ref 29, p. 139
42. Brenner, S., Miller, M. K., Soffa, W. A. 1982. *Scri. Metall.* 16:831
43. Zhu, F., von Alvensleben, L., Haasen, P. 1984. *Scri. Metall.* 18:337